ՀՀ ԳԱԱ Վ. ՀԱՄԲԱՐՁՈՒՄՅԱՆԻ ԱՆՎԱՆ ԲՅՈՒՐԱԿԱՆԻ ԱՍՏՂԱԴԻՏԱՐԱՆ

Հարությունյան Գևորգ Գարեգնի

Մեծ հեռավորությամբ բլազարների բազմահաճախային ճառագայթման մեխանիզմների ուսումնասիրությունը

ՍԵՂՄԱԳԻՐ

Ա.03.02 - «Աստղաֆիզիկա, ռադիոաստղագիտություն»
մասնագիտությամբ ֆիզիկամաթեմատիկական գիտությունների թեկնածուի
գիտական աստիճանի հայցման ատենախոսության

ԵՐԵՎԱՆ-2023

NAS RA BYURAKAN ASTROPHYSICAL OBSERVATORY AFTER V. AMBARTSUMIAN

Harutyunyan Gevorg Garegin

Broadband study of high redshift blazars

Thesis for the degree of candidate in physical and mathematical sciences
Specialty 01.03.02 – “Astrophysics and Radioastronomy”

SYNOPSIS

YEREVAN-2023

Ատենախոսության թեման հաստատվել է ՀՀ ԳԱԱ Վ. Համբարձումյանի անվան Բյուրականի աստղադիտարանի գիտական խորհրդում:

Գիտական ղեկավար՝
ֆիզ.-մաթ. գիտ. դոկտոր Նարեկ Սահակյան
Պաշտոնական ընդդիմախոսներ՝
1. ֆիզ.-մաթ. գիտ. դոկտոր Գագիկ Տեր-Ղազարյան
2. ֆիզ.-մաթ. գիտ. թեկնածու Գրիգոր Ալավերդյան

Առաջատար կազմակերպություն՝
Երևանի Պետական Համալսարան (ԵՊՀ)

Պաշտպանությունը կայանալու է 2023 թ. հունիսի 22-ին ժամը 14:00-ին, ՀՀ ԳԱԱ Բյուրականի աստղադիտարանում գործող ՀՀ ԲՈԿ-ի «Աստղագիտություն» 048 մասնագիտական խորհրդի նիստում (0213, Բյուրական, Արագածոտնի մարզ):
Ատենախոսությանը կարելի է ծանոթանալ ՀՀ ԳԱԱ Վ. Համբարձումյանի անվան Բյուրականի աստղադիտարանի գրադարանում:
Սեղմագիրը առաքված է 2023 մայիսի 11-ին:

Մասնագիտական խորհրդի գիտական քարտուղար՝  ֆիզ.-մաթ. գիտ. թեկնածու Ելենա Նիկողոսյան

The subject of the dissertation is approved by the scientific council of the NAS RA Byurakan Astrophysical Observatory after V. A. Ambartsumian

Scientific advisor:
Doctor of Phys. Math. Sciences Narek Sahakyan
Official opponents:
1. Doctor of Phys. Math. Sciences Gagik Ter-Kazarian
2. Candidate of Phys. Math. Sciences Grigor Alaverdyan
Leading Organization:
Yerevan State University

The defence will take place on 22nd of June 2023 at 14:00 at the meeting of the specialized council of the SCC 048 “Astronomy” of the Byurakan Astrophysical Observatory named after V. Ambartsumian NAS RA (0213, Byurakan, Aragatzotn Prov.).
The dissertation can be found at the Byurakan Astrophysical Observatory library.
The synopsis has been sent out on 11th of May, 2023.

Scientific secretary of the Special Council  Candidate of Phys. Math. Sciences Elena Nikighosyan

Modernity

The progression of technology in both space and ground-based detectors has now opened up unprecedented opportunities for exploring astrophysical objects across a wide range of energy bands. These include radio, infrared, optical, ultraviolet, X-ray, and γ-ray bands. Various objects are known to have non-thermal emission ranging from radio to High Energy (HE; > 100 MeV) and/or Very High Energy (VHE) γ-ray bands. Among these objects are different types of Active Galactic Nuclei (AGNs), which are very luminous sources. The radiation is primarily generated from a compact core that significantly dominates over the emission from the other parts of galaxy.

Approximately 10% of AGNs are classified as radio loud, and these exhibit a narrow beam of plasma, called a jet, that is ejected from the central region of a supermassive black hole. These jets remain collimated and their narrow structure can extend to larger distances, sometimes to kiloparsec or even megaparsec scales. The jet, composed of highly energetic particles such as electrons and positrons accelerated to relativistic speeds, plays an important role in the study and classification of AGNs. The appearance of radio-loud AGNs can vary greatly depending on the orientation of their jets. If the jet is oriented at a small angle with respect to the observer, the AGN is classified as a blazar.

Blazars are a subclass of AGNs that exhibit some of the most extreme properties in the universe, making them fascinating objects for astrophysical research. They can be further classified into two subtypes: flat-spectrum radio quasars (FSRQs) and BL Lacertae objects (BL Lacs) depending on the emission lines. FSRQs are characterized by the strong emission lines which are absent or very weak for BL Lacs. Blazars are known for their rapid and extreme variability across all energy bands, ranging from radio to γ-ray bands. The variability timescales can be as short as minutes to hours, and this rapid change in flux is thought to be related to the relativistic jets and their orientation toward the observer.

Blazars are considered the most luminous and intriguing class of AGNs due to their unique and extreme characteristics. They are the brightest persistent sources in the universe and are visible even at great distances. This makes them of significant interest to astronomers and astrophysicists. Blazars at high redshifts ($z > 2.5$) are particularly important to study for several reasons: 1) high redshift blazars are some of the most distant known objects in the universe, allowing to examine the early universe and the formation of the first galaxies, 2) the strong radiation from blazars will enable to understand the intergalactic medium, particularly the distribution of gas in the universe, 3) studying these objects helps to investigate the cosmological evolution of blazars and supermassive black holes, 4) large distances to high redshift blazars can be used to constrain cosmological parameters, such as the density of extragalactic background light (EBL), 5) can shed light on evolution of relativistic jets across different cosmic epochs and accretion disc-jet connection. Recently, multiwavelength observations have identified new high redshift blazars, and the availability of a substantial amount of multiwavelength data has increased, allowing for their detailed study. Studying these objects can provide valuable insights into various astrophysical phenomena, such as the processes occurring near supermassive black holes, the acceleration and interaction of relativistic particles, and the large-scale structure and evolution of the

universe. So, the broadband investigation of high redshift blazars has become one of the interesting topics in modern high-energy astrophysics.

Research goals and tasks

The aim of the thesis is to study the multiwavelength emission properties of high redshift blazars detected in the HE γ-ray band. For this purpose, a large amount of multiwavelength data is analyzed, and different theoretical models are applied. In particular, the main goals are:

1. to investigate the spectral and temporal properties of 33 distant blazars ($z > 2.5$) detected in the HE γ-ray band by analyzing the Fermi-LAT and Swift UVOT and XRT data.

2. to study the multi-frequency spectral and temporal properties of high redshift blazar PKS 0537-286 by analyzing data from Fermi-LAT, NuSTAR, Swift XRT, and UVOT observations, and investigate the origin of broadband emission by applying a one-zone leptonic scenario, assuming different locations of the emission region.

3. to investigate the γ-ray flaring activities of blazar B3 1343+451 ($z = 2.534$) by analyzing data accumulated between August 4, 2008, and August 4, 2018, and performing detailed temporal analysis.

4. to study the origin of broadband emission from high redshift blazars PKS 1830-211 ($z = 2.507$), LQAC 247-061 ($z = 2.578$), 4C +41.32 ($z = 2.550$), PKS 2311-452 ($z = 2.884$), PMN J0833-0454 ($z = 3.450$), PKS 2318-087 ($z = 3.164$), and TXS 0536+145 ($z = 2.690$) by analyzing all the available multiwavelength data.

Scientific novelty

The broadband study of emission from all 33 high redshift blazars ($z > 2.5$) observed in the HE γ-ray band showed that in the $\Gamma_\gamma - L_\gamma$ plane, the majority of the considered sources occupy the narrow range of $\Gamma_\gamma = 2.2 - 3.1$ and $L_\gamma = (0.10 - 5.54) \times 10^{48}$ erg s^{-1}, which is more typical for the brightest blazars. However, during γ-ray flares, the luminosity of variable sources is significantly beyond this boundary, changing within $10^{49} - 10^{50}$erg s^{-1}. The black hole mass estimated for the sources with a clear blue-bump in their Spectral nergy Distribution (SED) is in the narrow range of $(1.69 - 5.35) \times 10^9$ $M_\odot$ where the highest black hole mass of 5.35×10^9 $M_\odot$ is estimated for PMN J0226+0937 which has also the highest disc luminosity. Several periods are identified when the γ-ray photon index of blazars at the high redshift hardened; the hardest γ-ray spectra of B3 1343+451, B3 0908+416B and TXS 0907+230 are with indexes of 1.73 ± 0.24, 1.84 ± 0.25, and 1.72 ± 0.15, respectively, while that of TXS 0536+145 and 4C+41.32 was $\Gamma_\gamma = 2.00 \pm 0.16$ and $\Gamma_\gamma = 2.10 \pm 0.11$ respectively. In the γ-ray emission of PKS 0537-286 multiple powerful γ-ray flares were observed. Starting from MJD 59170, the source was in an enhanced γ-ray emission state when the γ-ray luminosity reached 6.14×10^{49} erg s^{-1}. During the considered fourteen years, the γ-ray luminosity of the source exceeded 10^{49} erg s^{-1} for 61.8 days in total. The modeling of the SED of B3 1343+451 in the quiescent state allowed to constrain the properties of the jet when it is in the average emission state. The flares can be reproduced by changing the bulk Lorentz factor of the emission region and slightly changing the energy distribution of the emitting electrons, the total luminosity of the jet being constant.

Practicality of the research

In this thesis, novel analysis methods were applied to develop a tool for the automatic analysis of γ-ray data observed by Fermi-LAT. As the amount of data observed by Fermi-LAT continuously increases, its automated analysis is crucial for performing both spectral and temporal analyses. The light curves and SEDs in different periods obtained from the multiwavelength study of high redshift blazars are important for further investigating these powerful objects. The parameters estimated from the theoretical modeling of SEDs for a large sample of high redshift blazars can be used to study the evolution of blazar jets (plasma, magnetic field, etc.) in the early epoch of the universe. The results from theoretical modeling of PKS 0537-286 SEDs in quiescent and flaring periods are significant for investigating where the energy dissipation of the jet occurs. The temporal analysis of the γ-ray light curve of B3 1343+451 is crucial for understanding the size of the emitting region and can be used in further modeling of blazar SEDs.

Key points presented to defend

1. It is shown that the considered 33 high redshift blazars have soft time-averaged γ-ray spectra ($\Gamma_\gamma \geq 2.2$) whereas those that have been observed in the X-ray band have hard X-ray spectra ($\Gamma_X = 1.01 - 1.86$). The γ-ray flux of high redshift blazars ranges from 4.84×10^{-10} to 1.50×10^{-7} photon $cm^{-2}s^{-1}$and the luminosity is within $(0.10 - 5.54) \times 10^{48}$ erg s^{-1} which during the γ-ray flares increases up to $(0.1 - 1) \times 10^{50}$ erg s^{-1}. In the X-ray band, only the emission of PKS 0438-43, B2 0743+25, and TXS 0222+185 varies in different Swift XRT observations whereas γ-ray emission is variable for fourteen sources (e.g., the flux of B3 1343+451 and PKS 0537-286 changes in sub-day scales, that of PKS 0347-211 and PKS 0451-28 in day scales). From the fitting broadband SEDs, the emission region size is found to be ≤ 0.05 pc and the magnetic field and the Doppler factor are correspondingly within $0.10 - 1.74$ G and $10.0 - 27.4$ while the central black hole masses and accretion disc luminosities are within $(1.69 - 5.35) \times 10^9$ $M_\odot$ and $L_d \simeq (1.09 - 10.94) \times 10^{46}$ erg s^{-1}, respectively.
2. The time averaged γ-ray spectrum of PKS 0537-286 is relatively soft (indicating the HE emission peak is below the GeV range) but several prominent flares were observed when the spectrum hardened and the luminosity increased above 10^{49} erg s^{-1}. The X-ray emission of the source varies in different observations and is characterized by a hard spectrum ≤ 1.38 with a luminosity of $> 10^{47}$erg s^{-1}. By comparing the model parameters from the modeling the broadband SEDs during the quiescent and flaring periods, it is shown that the most optimistic scenario is when the jet energy dissipation occurs within the broad-line region and the flaring activities are most likely caused by the hardening of the emitting electron spectral index and shifting of the cut-off energy to higher values.
3. The γ-ray emission from B3 1343+451 was flaring on 05 December 2011 and on 13 December 2009 when the flux increased up to $(8.78 \pm 0.83) \times 10^{-7}$ photon $cm^{-2}s^{-1}$. The hardest photon index $\Gamma = 1.73 \pm 0.24$ has been observed on MJD 58089 which is not common for FSRQs. In 2014 the X-ray flux of the source increased ~2 times as

compared to 2009, but in both periods the X-ray emission is characterized by a hard photon index of $\Gamma_{\mathrm{X-ray}} = 1.2 - 1.3$. The shortest flux halving timescale was estimated to be ~2.34 days, implying the emission had been produced in a very compact region, $R \leq \delta \times c \times t/(1+z) = 3.43 \times 10^{16}$cm (when $\delta = 20$).

4. It is found several flaring periods with significant increases in flux and hardening of the photon index in the HE γ-ray band for PKS 1830-211, LQAC 247-061, TXS 0536+145, and 4C+41.32. PKS 1830-211 was in an extraordinarily bright state on MJD 58596.49 when the 3-day averaged flux increased up to $(1.74 \pm 0.04) \times 10^{-5}$ photon $\mathrm{cm}^{-2}\mathrm{s}^{-1}$. The X-ray emission of PKS 1830-211 is also strongly variable and is characterized by a hard photon index in the range of $0.34 - 0.94$.

Approbation of the work

The results of the thesis were presented in Sixteenth Marcel Grossmann Meeting MG16 (Virtual Meeting - July 5-10, 2021) as well as frequently presented and discussed at the seminars of ICRANet Armenia center IO.

Publications

Four articles and one proceeding are published on the topic of the thesis.

Structure of the thesis

The thesis consists of Introduction, five chapters, conclusion and References. The thesis contains 120 pages, including 23 figures and 12 tables.

Content

In the **Introduction**, an overview of blazar properties is provided, followed by an outline of the scientific novelty of the thesis. Additionally, a brief summary of each chapter is given.

In **chapter 1** the primary steps for analyzing γ-ray data observed by the Fermi-LAT is presented. It includes a detailed explanation of the automatic tool designed for data analysis, as well as a brief overview of the emission processes occurring within blazar jets.

In **chapter 2** the multiwavelength emission properties of all the thirty-three known γ-ray blazars beyond redshift 2.5 was investigated. A small fraction (1.18%) of blazar in the fourth catalog of AGNs detected by Fermi-LAT are distant blazars $z > 2.5$(~ 20.7 Gpc), including 26 FSRQs, two BL Lacs and five blazars of uncertain type (BCU). The multiwavelength propertis of these distant blazars was investigated by performing detailed spectral and temporal analysis of Fermi-LAT γ-ray data accumulated during 2008-2018 and by analyzing both Swift X-ray Telescope (XRT) and Ultraviolet/Optical Telescope (UVOT) data accumulated in the previous fifteen years.

The γ-ray properties of the selected sources were investigated by analyzing Fermi-LAT data accumulated during the first 10 yr of operation, from 2008 August 4 to 2018 August 4. The PASS 8 events from a circular region with a radius of 12° around each source in the

energy range from 100 MeV to 500 GeV were downloaded and analyzed with the Fermi Tools (1.2.1) using P8R3 instrument response functions. The γ-ray light curves are calculated using the unbinned likelihood analysis method implemented in the gtlike tool. Initially, in order to study the variability, the γ-ray light curves with 30-day binning are calculated for all sources, considering the $0.1 - 300$ GeV range. Additionaly light curves with short periods (days or a week) were computed for the statistically significant ($\geq 5\sigma$) γ-ray emitting periods identified in the monthly light curves. Next, the γ-ray variability is studied further using the adaptively binned method.

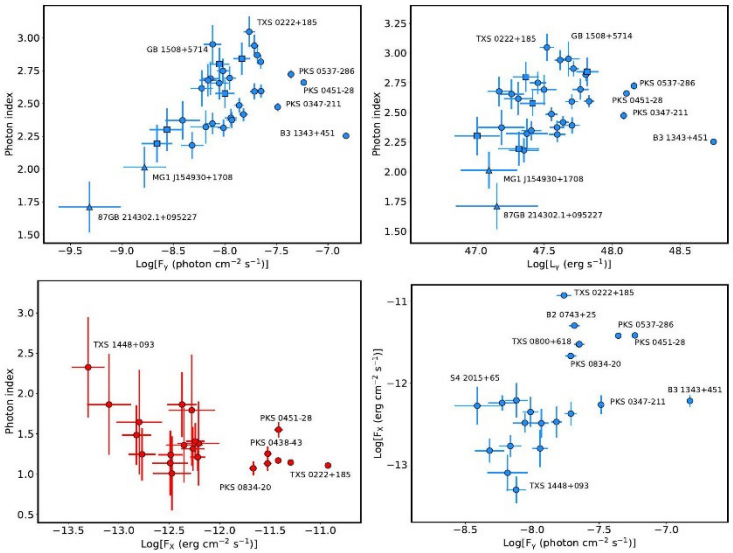

Figure 1. The γ-ray flux (> 100 MeV) and luminosity of considered sources versus the photon index are shown in the upper panels. BL lacs, FSRQs and BCUs are shown with triangles, circles, and squares, respectively. Lower left panel: The X-ray flux (0.3-10 keV) versus the photon index. Lower right panel: Comparison of γ-ray and X-ray (if available) fluxes.

Swift is a multi-frequency space observatory, designed to study the sources in optical/UV and X-ray bands. Twenty-nine sources from considered sources (except MRSS 291081526, CRATES J233930+024420, MG1 J154930+1708 and B3 1624+414) were at least once observed by Swift. There are available data from multiple observations of some sources; e.g., B2 0743+25, PKS 0438-43, TXS 0222+185, TXS 1448+093, PMN J0226+0937, TXS 1616+517 and PKS 2107-105 had been observed more than ten times. The Swift XRT data analysis was possible to apply only for twenty-two sources and twenty-six were detected in at least one of the optical-UV Swift-UVOT filters.

In Figure 1 The γ-ray photon index versus flux (estimated from power-law fitting) is shown in the upper left panel, where the FSRQs are circles, BL Lacs triangles and BCUs squares. The photon index $\left(\sim E^{-\Gamma_\gamma}\right)$ estimated in the 0.1-500 GeV range ranges from 1.71 to

3.05 with a mean of 2.54. The soft γ-ray spectra of the considered sources (except 87 GB 214302.1+095227 and MG1 J154930+1708) indicate that the peak of the HE component in their SEDs is in the MeV range. The flux of considered sources ranges from 4.84×10^{-10} to 1.50×10^{-7} photon $cm^{-2}s^{-1}$. The two BL Lacs detected beyond $z = 2.5$, 87GB 214302.1+095227 and MG1 J154930+1708, have the lowest flux, $(4.84 \pm 1.37) \times 10^{-10}$photon $cm^{-2}s^{-1}$ and $(1.66 \pm 0.79) \times 10^{-9}$ photon $cm^{-2}s^{-1}$, respectively, but they have a harder γ-ray spectrum. The γ-ray flux of BCUs included in the sample ranges from 2.19×10^{-9} photon $cm^{-2}s^{-1}$ to 1.46×10^{-8} photon $cm^{-2}s^{-1}$ with Γ_γ within $2.20 - 2.84$. The FSRQs occupy the region of high flux $\geq 3.89 \times 10^{-9}$ photon $cm^{-2}s^{-1}$ and $\Gamma_\gamma \geq 2.2$ with a mean $F_\gamma \simeq 2.11 \times 10^{-8}$ photon $cm^{-2}s^{-1}$. The highest γ-ray flux of $(1.50 \pm 0.02) \times 10^{-7}$ photon $cm^{-2}s^{-1}$ was observed from the bright FSRQ B3 1343+451.

The flux, which is a function of the distance, is compared for each source in Figure 1 (upper left panel). Even though it is informative, the total energy released from each source cannot be investigated. Next, using the observed flux (F_γ) and photon index (Γ_γ), the luminosity of each source is computed as:

$$L_\gamma = 4\pi d_L^2 \frac{\Gamma_\gamma - 1}{\Gamma_\gamma - 2} \frac{E_{max}^{2-\Gamma_\gamma} - E_{min}^{2-\Gamma_\gamma}}{E_{max}^{1-\Gamma_\gamma} - E_{min}^{1-\Gamma_\gamma}} F_\gamma \quad (1)$$

where $E_{min} = 100$ MeV and $E_{max} = 500$ GeV. Figure 1 (upper right panel) shows the distribution of the considered sources in the $\Gamma_\gamma - L_\gamma$ plane. The γ-ray luminosity of considered sources ranges from 1.01×10^{47} erg s^{-1} to 5.54×10^{48} erg s^{-1}. The lowest luminosity of $(1.01 \pm 0.38) \times 10^{47}$ erg s^{-1} has been estimated for CRATES J105433+392803 which is of the same order with that of the two BL Lacs included in the sample; $(1.42 \pm 0.98) \times 10^{47}$ erg s^{-1} for 87GB 214302.1+095227 and $(1.24 \pm 0.59) \times 10^{47}$ erg s^{-1} for MG1 J154930+1708. The γ-ray luminosity of only PKS 0347-211, PKS 0451-28, PKS 0537-286 and B3 1343+451 exceeds 10^{48} erg s^{-1} with the highest γ-ray luminosity of $(5.54 \pm 0.06) \times 10^{48}$ erg s^{-1}, estimated for B3 1343+451. The X-ray flux is plotted versus the photon index in the lower left panel of Figure 1. For several sources, the number of detected counts was not high enough, so the flux and photon index were estimated with large uncertainties. The X-ray photon index of considered sources is < 2.0, implying the X-ray spectra have a rising shape in the $\nu F\nu \sim \nu^{2-\Gamma_X}$ representation, which is natural as LSP blazars are considered. B3 0908+416B has the hardest X-ray spectrum with $\Gamma_X = 1.01 \pm 0.46$. In the $F_X - \Gamma_X$ plane, PKS 0451-28, TXS 0222+185, PKS 0834-20, PKS 0537-286, TXS 0800+618, B2 0743+25 and PKS 0438-43 are detached from the other sources because they have a comparably high X-ray flux, $F_{X-ray} \geq 2.13 \times 10^{-12}$ erg $cm^{-2}s^{-1}$. In the lower right panel of Figure 1 the γ-ray and X-ray (if available) fluxes of the considered sources are compared. Interestingly, the bright γ-ray sources PKS 0537-286 and PKS 0451-28 appear to be also bright X-ray emitters. The other bright γ-ray blazars (e.g., B3 1343+451, PKS 0451-28) do not

have any distinguishable feature in the X-ray band, having a flux and photon index similar to those of the other considered sources. The bright X-ray sources TXS 0222+185, B2 0743+25, TXS 0800+618, and PKS 0834-20 appear with a similar flux in the γ-ray band, $F_\gamma = (1.72 - 2.23) \times 10^{-8}$ photon $cm^{-2}s^{-1}$.

To understand the origin of the broadband emission of the considered sources, a simple one-zone leptonic model was used. In this model, the emission region is assumed to be a spherical blob of radius of R moving in the blazar jet with a bulk Lorentz factor of Γ_j at a viewing angle of θ. The emitting region is filled with a uniformly tangled magnetic field B and with a homogeneous population of relativistic electrons (and positrons), the nonthermal energy distribution of which is described by a power-law with an exponential cut-off at higher energies as:

$$N(\gamma) \sim \gamma^{-\alpha}\, exp\left(-\frac{\gamma}{\gamma_{\rm cut}}\right)\ \gamma > \gamma_{min} \quad (2)$$

where γ is the Lorentz factor of electrons in the blob rest frame, and α is the power-law index. $\gamma_{\rm min}$ and $\gamma_{\rm cut}$ are the Lorentz factors corresponding to the minimum and cutoff energy of the electron distribution in the emission region.

In the modeling it is assumed that the low-energy peak (from radio to optical/UV) is due to synchrotron emission from ultra-relativistic electrons in the jet with an energy distribution as given by Eq.2. Instead, the HE peak is due to the IC scattering of internal (SSC) or external photons (EIC). The IC scattering of external photons is considered, since the SEDs of FSRQs are better explained by EIC, as shown by the previous studies and the CD is evident in the SEDs of the considered sources. Here we assume that the emitting region is outside the broad-line region (BLR) where the dominant photon field is the IR emission from the dusty torus. The IR radiation from the dusty torus is assumed to have a blackbody spectrum with a luminosity of $L_{IR} = 0.6L_{disc}$ where L_{disc} is the accretion disk luminosity, which fills a volume that is approximated as a spherical shell with a radius of $R_{IR} = 2.5 \times 10^{18}(L_d/10^{45})^{1/2}$ cm.

Some of the SEDs modeling results are presented in Figure 2. The applied model reproduces the multiwavelength data relatively well for almost all the sources. The electron power-law index is defined by the X-ray data (through $\alpha = 2\Gamma_X - 1$ relation) and depending on whether the SSC or EIC component is dominating in the X-ray band, different values for α are obtained. When the X-ray spectrum is hard and the SSC component is dominating, the energy distribution of the emitting electrons has a hard spectrum as well. For example, for GB 1508+5714, PKS 0537-286, B2 0743+25, TXS 0222+185 and B3 0908+416B, $\alpha = 1.17 \pm 0.07,\ 1.33 \pm 0.07,\ 1.13 \pm 0.19,\ 1.62 \pm 0.05$ and 1.31 ± 0.25 were estimated which shows that the emission is due to newly accelerated electrons. On the contrary, when the emission in the X-ray and γ-ray bands is only defined by the EIC component then $\alpha > 2.2$; e.g., $\alpha = 2.75 \pm 0.04$ and 2.70 ± 0.06 are correspondingly estimated for TXS 0800+618 and PKS 0834-20. Correspondingly, $\gamma_{\rm min}$ and $\gamma_{\rm cut}$ are in the range of $2.58 - 93.28$ and $(1.01 - 15.73) \times$

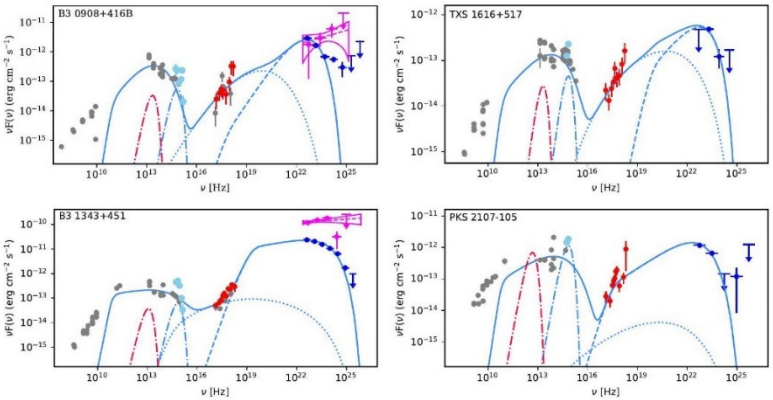

Figure 2. Modeling of the broadband SEDs of some sources. The Swift UVOT, XRT and Fermi-LAT data obtained here are shown with cyan, red and blue, respectively, while the archival data are in gray.

10^3 (excluding TXS 1448+093). As expected, lower values of γ_{min} are estimated when the X-rays are produced only by the EIC component: e.g., $\gamma_{min} = 2.68 \pm 0.36$ and 2.58 ± 0.15 are correspondingly estimated for PKS 1351-018 and OD 166. The HE tails of both synchrotron and IC components are well defined by the optical/UV and γ-ray data, respectively, allowing precise estimation of $\gamma_{cut} = (1.01 - 15.73) \times 10^3$. γ_{cut} is in a strong dependence on α, and its highest value, $(15.73 \pm 1.60) \times 10^3$ was estimated when $\alpha = 2.80 \pm 0.04$. Meanwhile, when $\alpha = 2.2 - 2.5$, the highest γ_{cut} is $(8.67 \pm 0.48) \times 10^3$ for B3 1343+451. The modeling shows that the magnetic field in the emitting region is within $0.10 - 1.74$ G. The estimated Doppler factor is from $\delta = 10.00$ to $\delta = 27.42$ with a mean of $\delta = 19.09$. Although, these are higher than the average values estimated for FSRQs, they are well within the range of physically realistic values. The emitting region size is within $R = (0.70 - 9.48) \times 10^{16}$ cm except for TXS 0800+618 and S4 2015+65 for which $R = 1.55 \times 10^{17}$ cm and 1.35×10^{17} cm, respectively. The values estimated for R are consistent with the γ-ray flux variation in a day or several day scales and suggest that the multiwavelength emission is produced in the sub-parsec scale regions of the jet.

In **chapter 3** the broad band study of one of the brightest high redshift blazars PKS 0537-286; at $z = 3.10$ is performed. The γ-ray data collected between 2008 August 4 and 2022 September 9 (MET=239557417–686130659) were analyzed. In order to investigate the variability pattern of the source, the light curves were computed with 5-day bins as well as with the help of adaptive binning method. The adaptively binned light curve ($> E_{opt} = 168.19$ MeV) is shown in Figure 3 upper panel. Up to MJD 57740 the γ-ray flux was in its average level of $(1 - 3) \times 10^{-8}$ photon $cm^{-2}s^{-1}$ with no significant changes, while then, in several occasions, the γ-ray flux increased substantially. The light curve with 5-day (> 100 MeV) and adaptive bins ($> E_{opt} = 168.19$ MeV) for the period when the source was active in the γ-ray band are shown correspondingly in Figure 3 panels (a) and (b). The first

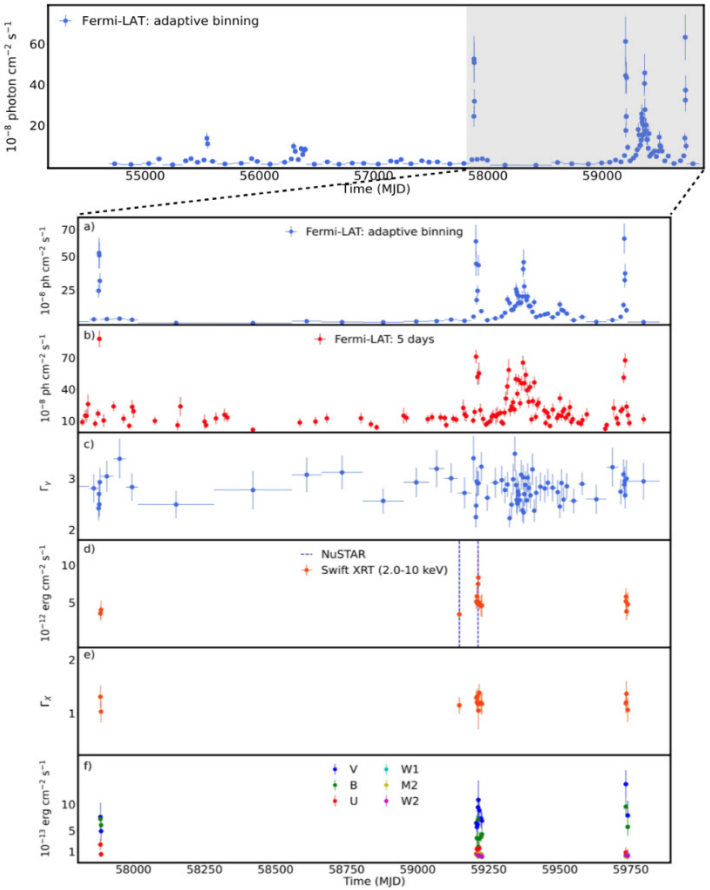

Figure 3. Multiwavelength light curve of PKS 0537-286. Top panel shows the long-term adaptively binned γ-ray light curve above 168.19 MeV. The other panels show the light curves after MJD 57800 (16 February 2017) when the source was active in the γ-ray band.

flaring period was between MJD 57876-57883 when the flux increased with a maximum of $(5.26 \pm 1.13) \times 10^{-7}$ photon $cm^{-2}s^{-1}$. Starting from MJD 59170, the source entered an active emission state with several bright flaring periods between MJD 59204-59233, MJD 59301-59411 and MJD 59721-59738. The maximum γ-ray flux of the source, $(6.32 \pm 1.11) \times 10^{-7}$ photon $cm^{-2}s^{-1}$ was also observed in these γ-ray flaring periods. Figure 3 panel (c) shows the γ-ray photon index estimated for the adaptively binned periods; it varies in time as well. In the non-flaring periods, the γ-ray spectrum is characterised by a soft spectrum with a mean of $\Gamma \simeq 2.83$ but the photon index hardens during the bright periods as can be seen from Figure 3 panel (c). For example, during the first flare between MJD 57876-57883 the hardest index of 2.49 ± 0.23 was observed on MJD 57879.9 or during the second flare between MJD 59204-59233 the hardest index was 2.25 ± 0.21 when the

source was in an active state with a flux of $(6.12 \pm 1.22) \times 10^{-7}$ photon $cm^{-2}s^{-1}$. During the hardest γ-ray emission period, 2.23 ± 0.18 was detected on MJD 59322 which is unusual for this source.

All the XRT observations were processed with Swift_xrtproc tool applying standard analysis procedure. The 2-10 keV X-ray flux variation is shown in Figure 3 panel (d). The X-ray emission of the source in the $2.0 - 10$ keV band was at the level $\sim 3.0 \times 10^{-12}$ erg $cm^{-2}s^{-1}$ but during the bright periods it is $\geq 5.0 \times 10^{-12}$ erg $cm^{-2}s^{-1}$. The highest X-ray flux of $(8.34 \pm 3.59) \times 10^{-12}$ erg $cm^{-2}s^{-1}$ was observed on MJD 59213.18. The X-ray spectrum of the source is hard (Figure 3 panel (e)) and during all the observations $\Gamma_{X-ray} \leq 1.38$.

The analyzed data allows to build the SEDs of PKS 0537-286 in different periods. The SED/light curve animation is available here https://youtu.be/4UPqf-C7EWcyoutube.com/4UPqf-C7EWc. In order to understand the origin of emission processes, the SEDs from following periods were considered for modeling:

(i) between MJD 55150-55330 when the source was in the quiescent state.

(ii) between MJD 59208-59212 when the source was bright in the γ-ray and X-ray bands.

The broadband SEDs were modeled using a one-zone leptonic scenario. In order to have a general view we consider three different scenarios: i) the broadband emission from PKS 0537-286 is entirely due to synchrotron/SSC radiation, ii) the jet dissipation region is close to the central black hole, and SSC, EIC-disk and EIC-BLR are contributing to the HE component and iii) the emission region is beyond the BLR and the HE component is due to EIC-torus. It is assumed that BLR is a spherical shell with lower and upper boundaries of $0.9 \times R_{BLR}$ and $1.2 \times R_{BLR}$, respectively. R_{BLR} is assumed to scale as $R_{BLR} = 10^{17} L_{disc,45}^{0.5}$cm where $L_{disc,45} = \frac{L_{disc}}{10^{45}}$ erg s^{-1} is the accretion disk luminosity. Similarly, we assume that the distance of dusty torus is $2 \times 10^{18} L_{disc,45}^{0.5}$ which emits $\eta = 0.5$ fraction of disk luminosity in the IR range for which we adopted $T_{torus} = 10^3$ K effective temperature. The disk luminosity and effective temperature are correspondingly 8.7×10^{46} erg s^{-1} and $T_{disk} = 1.9 \times 10^4$ K estimated by fitting the thermal blue-bump component in the SED with a black-body component. Figure 4 panels (a) and (b) show the results of the modeling when the entire emission is due to synchrotron/SSC emission from a compact region of the jet when the source is in a quiescent and flaring state, respectively. In the quiescent state the spectral slope of the emitting particle distribution is 1.8 ± 0.1 and their distribution extends up to $(1.2 \pm 0.1) \times 10^4$. The strength of the magnetic field is found to be $(9.3 \pm 0.8) \times 10^{-3}$ G. The emission region size is $(2.0 \pm 0.1) \times 10^{17}$ cm, which is consistent with the flux variability of $t_{var} = (1 + z) \times \frac{R}{c} \delta \approx 18.7$ days. The Doppler boosting factor is 16.8 ± 1.2. In the flaring period (Figure 4 panel (b)), the SED modeling shows that the emitting electrons have a harder spectrum with $p = 1.6 \pm 0.03$. The electrons are accelerated up to $\gamma_{cut} = (1.1 \pm 0.1) \times 10^4$

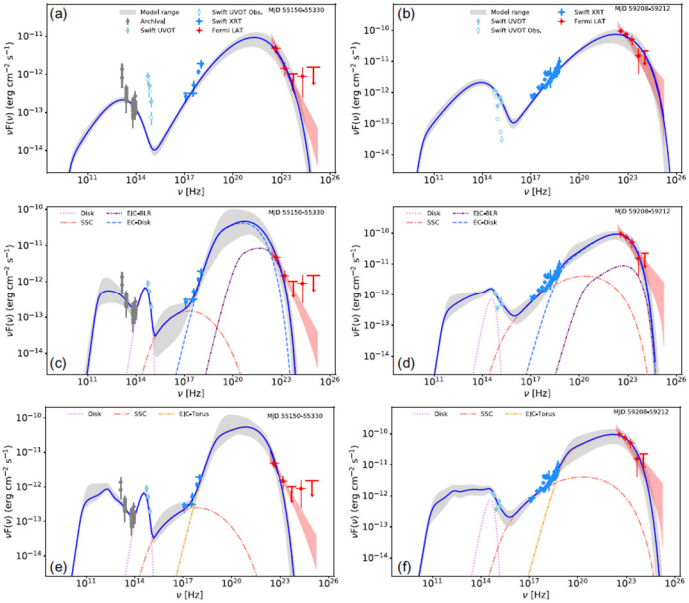

Figure 4. The broad-band SEDs of PKS 0537 –286 in the quiescent (left-hand panels) and flaring (right-hand panels) states.

which is not significantly different from that in the quiescent state. In the flaring state, the magnetic field also increased, $B = (1.7 \pm 0.1) \times 10^{-2}$ G, which is caused by the increase of the synchrotron flux. Also, the Doppler boosting factor increased from 16.8 ± 1.2 to 24.9 ± 1.1 in order to explain the slight shift of the HE peak towards higher energies.

Figure 4 panels (c) and (d) show the SED modeling assuming the jet dissipation occurred close to the central source. The thermal emission from the accretion disk, modeled as a black body, is shown with a pink dashed line. The distribution of the electrons is narrower with $p = 2.3 \pm 0.2$ and $\gamma_{cut} = (0.3 \pm 0.1) \times 10^3$, because the average energy of the external photons is larger than that of the synchrotron one. The Doppler boosting factor is $\delta = 13.4 \pm 1.3$ but the magnetic field is significantly larger, $B = 3.5 \pm 0.4$ G. The emission is produced in a more compact region with a radius of $(0.2 \pm 0.02) \times 10^{17}$ cm, smaller than $R_{BLR} = 9.3 \times 10^{17}$cm. During the flaring period (Figure 4 panel (d)) the electron distribution is nearly flat with $p = 2.2 \pm 0.1$ and extends up to $(2.5 \pm 0.2) \times 10^3$. The increase of the energy up to which the electrons are effectively accelerated (γ_{cut}) resulted in the shift of the synchrotron component to higher frequencies and domination over the disk thermal emission. The Doppler boosting is $\delta = 11.4 \pm 0.7$, the magnetic field is $B = 3.0 \pm 0.2$ G and the emission region radius is $(0.1 \pm 0.01) \times 10^{17}$cm.

Figure 4 panels (e) and (f) show PKS 0537-286 SED modeling assuming the emission region is beyond the BLR. In the quiescent state, the HE component is entirely dominated by

EIC-torus (yellow dot-dot- dashed line in Figure 4 panel e) and SSC contributing in the soft X-ray band (orange dot-dashed line in Figure 4 panel e). The model parameters show that in the quiescent and flaring states the electron distribution has a similar power-law index $p \simeq 2.4$, but in the flaring state the cut-off energy is larger, $\gamma_{cut} = (6.7 \pm 0.7) \times 10^3$ as compared to $\gamma_{cut} = (1.3 \pm 0.1) \times 10^3$. Also, the modeling shows that the Doppler boosting and magnetic field do not substantially change, correspondingly being $\delta = 15.3 \pm 0.7$ and $B = 0.2 \pm 0.01$ G and $\delta = 14.2 \pm 1.0$ and $B = 0.2 \pm 0.02$ G for the flaring and quiescent states.

The parameters estimated during the modeling are used to compute the jet luminosity. The jet power carried by the electrons, calculated as $L_e = \pi c R_b{}^2 \Gamma^2 U_e$, and by magnetic field, calculated as $L_B = \pi c R_b{}^2 \Gamma^2 U_B$. When the emit- ting region is within the BLR, a lower jet luminosity is required, $L_e + L_B = 6.3 \times 10^{45}$ erg s^{-1} and $L_e + L_B = 2.5 \times 10^{45}$ erg s^{-1} for the quiescent and flaring states, respectively, and the system is close to equipartition with $L_e/L_B = 0.5$ and $L_e/L_B = 3.7$ for the quiescent and flaring states, respectively.

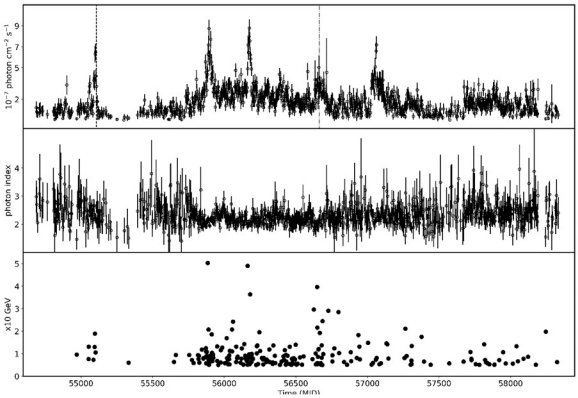

Figure 5. The evolution of γ-ray flux and spectral index of B3 1343+451 in time computed using 3-day bins.

In the **chapter 4** the γ-ray properties of B3 1343+451 are investigated by analyzing the data set collected during the first ten years of Fermi-LAT operation, from August 4, 2008, to August 4, 2018 (MET 239557417-555033605). The light curve of the source is shown in Figure 5. Several bright γ-ray emission states of the source can be identified, namely from MJD 55083 to 55116, from 55839 to 55965, from 56160 to 56235 and from 57021 to 57126. Interestingly, during the prolonged γ-ray active period from MJD 55720 to 57230, not only two major flares from the source were observed but also the flux increased from its average level and remained so for nearly 500 days. The peak flux of $(8.78 \pm 0.83) \times 10^{-7}$ photon cm^{-2}s^{-1} with a photon index of $\Gamma = 2.02 \pm 0.07$ was observed on MJD 56175 within three days with a detection significance of 25.1 σ. Another substantial increase of the γ-ray flux has been observed on MJD 55893 when the flux was $(8.73 \pm 0.85) \times$

10^{-7} photon $cm^{-2}s^{-1}$ with $\Gamma = 2.10 \pm 0.08$ photon index and with 24.0 σ detection significance. The γ-ray photon index variation in time computed for three-day bins is shown in the middle panel of Figure 5. Most of the time, the photon index varies around its averaged value reported in 4FGL (2.14 from the log-parabolic fit), but in some periods hardening and softening are evident. The hardest photon index of $\Gamma = 1.73 \pm 0.24$ has been observed on MJD 58089 with 6.2 σ while the softest one 3.13 ± 0.31 was observed on MJD 57675.

During the three outbursts in the γ-ray band (the first three peaks in Figure 5 upper panel) the rising and decaying shapes of the flares can be well constrained by the data. The temporal evolution of each flare has been studied separately. For this purpose, a time profile fitting of these flares is performed by a sum of exponentials which gives the rise and decay times of each peak,

$$F(t) = F_c + F_0 \left(\exp\left(\frac{t_0 - t}{t_r}\right) + \exp\left(\frac{t - t_0}{t_d}\right) \right)^{-1} \quad (3)$$

where F_0 is the flux at t_0 representing the approximate flare amplitude, F_c is the quiescent

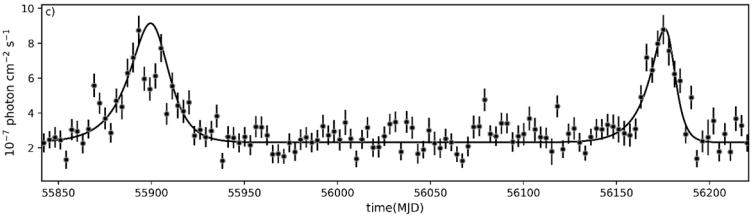

Figure 6. The flare time profile analyses.

flux, t_r and t_d are the rise and decay times of the flare, respectively. The light curve was fitted with the nonlinear optimization python package lmfit (https://lmfit.github.io/lmfit-py/).

The corresponding fit is shown in Figure 6. The two flares are fitted together with the same constant level of the flux to reduce the number of free parameters. These flares reach the peaks within 11.34 ± 2.85 and 9.21 ± 2.43 days, respectively, then the second one quickly drops to its average level within 3.64 ± 1.24 days while the decay of the other flare is relatively slow, 7.66 ± 2.19. The time peak of the flares are at MJD 55899.5 and MJD 56 175.98 with amplitudes of $(13.41 \pm 2.67) \times 10^{-7}$ and $(11.85 \pm 2.00) \times 10^{-7}$ photon $cm^{-2}s^{-1}$, respectively. The shortest flux doubling or halving timescales, computed by $t_{r,d} \times \ln 2$, is ~2.34 days.

The SED of B3 1343+451 during the quiescent (low), and flaring (F1 and F4) periods are shown in Figure 7. Initially, the SED in the quiescent state is modeled (Figure 7 left panel) to estimate the baseline energy of the jet as well as the radiating particle energy distributions. In this case, the X-ray to γ-ray data is interpreted as IC up-scattering of synchrotron (dot-dashed line in Figure 7 right panel) and torus (dashed line in Figure 7 right panel) photons.

The absence of high-quality X-ray data hardens the precise estimation of the power-law

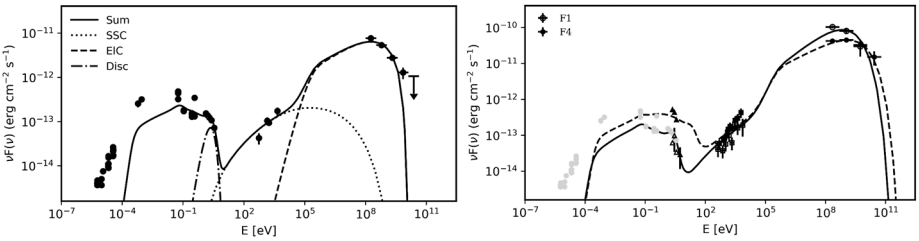

Figure 7. Modeling of the broadband SEDs of B3 1343+451 during the quiescent (left panel) and flaring states (F1 and F4 right panel).

index of the electrons and p = 2.39 is defined by SSC fitting to X-ray data. When $\gamma_{min} = 62.78$, $\gamma_{cut} = 4683.34$ and $\gamma_{max} = 1.04 \times 10^4$, the EIC component peaks around GeV energies, explaining the γ-ray data. In the emitting region, the magnetic field is B = 0.18 G with a density lower than that of electrons $U_e/U_B = 74.6$ which implies that even if the system is not perfect in equipartition ($U_e/U_B = 1$), there is no large deviation between electron and magnetic field energy densities. The multiwavelength SEDs during the flaring states are shown in Figure 7 (right panel).

During the fit, all the parameters describing the source (e.g., the luminosity of the torus, its radius, temperature, etc.) are fixed to the values obtained during the fit of the averaged state, while the parameters of the magnetic field and emitting electrons are left free to vary. X-ray to γ-ray data are again interpreted by the sum of SSC and EIC components (for the clarity only the sum of these components is depicted in Figure 7 right panel) and the X-ray spectra can be explained when p = 2.08 and p = 2.38 for the flares F1 and F4, respectively. As the γ-ray spectrum during F4 is characterized by a harder photon index which extends to higher energies, larger $\gamma_{cut} = 12095.01$ is estimated as compared with F1 ($\gamma_{cut} = 4884.00$). In order to account the increase on the γ-ray flux, higher energy densities of electrons are estimated which results in lower magnetic field (0.04 and 0.10 for F1 and F4, respectively) to keep the flux of the lower component at the same level since the synchrotron emission depends on the total energy of electrons and magnetic field. During the flaring states, the jet of B3 1343+451 becomes more particle dominated with $U_e/U_B > 900$, which is natural considering the ratio of IC to synchrotron luminosity increases.

In the **chapter 5** the properties of additional 7 high redshift blazar from Fermi-LAT catalogue based on 12 years of data have been investigated. The γ-ray properties of PKS 1830-211, LQAC 247-061, 4C +41.32, PKS 2311-452, PMN J0833-0454, PKS 2318-087, TXS 0536+145 were investigated by analyzing Fermi-LAT data accumulated between 2008 August 04 to 2022 December 04 (MET 239557417-691804805). After analyzing the data from the entire period, the γ-ray variability of the selected sources was investigated. Initially, the whole time period was divided into short equal periods or was constrained using adaptive binning method and the unbinned likelihood analysis was applied to estimate the flux and

the photon index. The γ-ray light curves of selected sources are shown in Figure 8. For each source, when the light curve generated with adaptively binning method is with a reasonable time bins, the light curves generated with fixed bins (circle) and with adaptive bins are shown. The light curves for PKS 1830-211 and LQAC 247-061 were downloaded from the Fermi-LAT Light Curve Repository[1], as the ROI around these sources contain a lot of objects making difficult the analysis. The most variable source in the sample is PKS 1830-211 (see panel a in Figure 8) which shows high amplitude flux changes in 3-day binned light curve. The γ-ray emission of this source increases time to time but the largest flare was observed during MJD 58572-58605 when the flux increased up to $(1.74 \pm 0.04) \times 10^{-5}$ photon $cm^{-2}s^{-1}$ on MJD 58596.49. It should be noted that average flux of γ-ray emission from this source is $(1.01 \pm 0.19) \times 10^{-6}$ photon $cm^{-2}s^{-1}$ so the flux increases ~17.22 times. The time averaged γ-ray spectrum of PKS 1830-211 is well explained with the index of $\Gamma_\gamma = 2.66 \pm 0.34$ but during the brightening the hardest index of $\Gamma_\gamma = 2.22 \pm 0.03$ was observed on MJD 58596.49. The γ-ray light curve of LQAC 247-061 with 7-day bins shows (panel b in Figure 8) several flaring periods although with smaller amplitudes as compared to PKS 1830-211: the maximum weekly flux of this source was $(5.87 \pm 1.34) \times 10^{-7}$ photon $cm^{-2}s^{-1}$ observed on MJD 59222.42. The adaptively binned light curve of TXS 0536+145 above 285.38 MeV (panel c Figure 8) shows that the source was in active emission state between MJD 55872-56138 when the flux above 285.38 MeV increased up to $(1.81 \pm 0.39) \times 10^{-7}$ photon $cm^{-2}s^{-1}$ on MJD 55945.22. On average the γ-ray spectral index of this source is around $\Gamma_\gamma = 2.68$ but during the flares occasionally it hardens, for example on MJD 56014.81 the index was $\Gamma_\gamma = 2.00 \pm 0.16$. Among the considered sources, the light curve generated with the help of adaptive binning method shows also 4C+41.32 has variable γ-ray emission (panel d in Figure 8); the averaged γ-ray flux of the source was $(3.24 \pm 0.94) \times 10^{-9}$ photon $cm^{-2}s^{-1}$ which increases up to $(5.75 \pm 0.12) \times 10^{-9}$ photon $cm^{-2}s^{-1}$on MJD 56177.66. It should be noted that during this bright period the photon index hardened being $\Gamma_\gamma = 2.10 \pm 0.11$. For the other remaining three sources (PKS 2311-452, PKS 2318-087 and PMN J0833-0454) no flux changes were observed in long- and short-time scales.

Among the considered sources, TXS 0536+145, PMN J0833-0454, LQAC 247-061 and PKS 1830-211 were at least once observed by Swift satellite. All these available data from XRT and UVOT observations were downloaded and analyzed. The XRT data were all processed using the Swift_xrtproc automatic tool. The 2.0-10 keV X-ray flux of PMN J0833-0454 is at the level of 1.86×10^{-13}erg $cm^{-2}s^{-1}$, instead, the spectral index is $\Gamma_X = 1.90 \pm 0.53$ and $\Gamma_X = 2.17 \pm 0.47$ which is unusually soft for FSRQs. Similarly, the 2.0-10 keV X-ray flux of

[1] https://fermi.gsfc.nasa.gov/ssc/data/access/lat/LightCurveRepository/

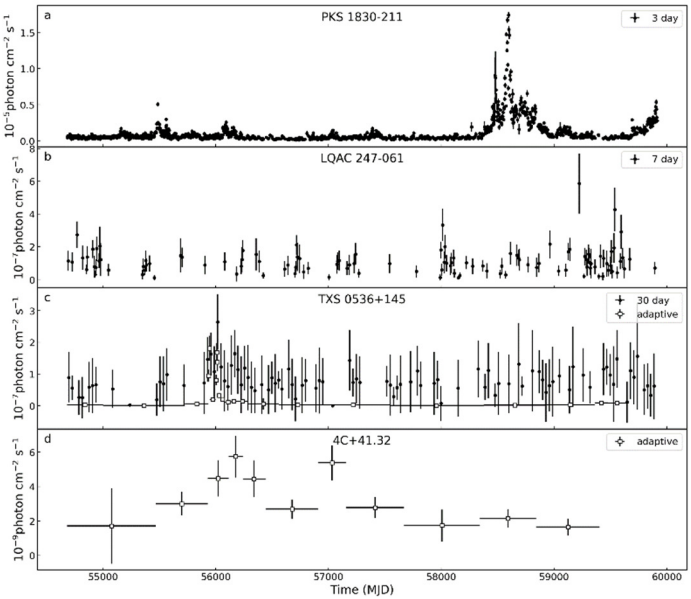

Figure 8. The γ-ray light curve of selected sources.

TXS 0536+145 and LQAC 247-061 is $(0.91-2.28)\times10^{-12}$ erg cm^{-2}s^{-1} and $(1.00-1.79)\times10^{-12}$ erg cm^{-2}s^{-1}, respectively, and their indexes are $1.45-1.88$ and $1.05-1.39$, respectively. PKS 1830-211 is the most variable source in the X-ray band. Thighest flux of $(2.41\pm0.44)\times10^{-11}$ erg cm^{-2}s^{-1} was observed on MJD 58583.10. The spectral index in the X-ray band is relatively hard, changing from 0.34 ± 0.14 to 0.94 ± 0.25, so it defines the rising spectrum of the HE component.

In order to investigate the origin of broadband emission from the considered sources, the data analyzed here were combined with the archival data retrieved using VOU-blazar tool. The SEDs composed with data retrieved from VOU-blazar tool and analyzed here, are shown in Figure 9. All the considered sources show the characteristic double peaked structure which is modeled within a leptonic one-zone scenario. The SEDs modeled with the synchrotron/SSC plus external Compton scattering of BLR photons is shown in Figure 9. The presented SEDs have sufficient data spanning from radio (archival) to HE γ-ray bands (analyzed here), which allows for shaping of both low and high energy peaks. The model utilized is able to effectively explain the multiwavelength data for nearly all of the sources. The modeling shows that multi wavelength data of PKS 1830-211, LQAC 247-061 and 4C+41.32 can be explained when the power-law index of emitting electrons is relatively hard, 1.79 ± 0.08, 1.97 ± 0.08, 1.74 ± 0.21 respectively. Whereas soft index of 2.96 ± 0.06 and 2.49 ± 0.07, respectively, are required to explain the data of TXS 0536+145 and PMN J0833-0454. Because of this soft index, the fit resulted to higher value for the cut-off energy for

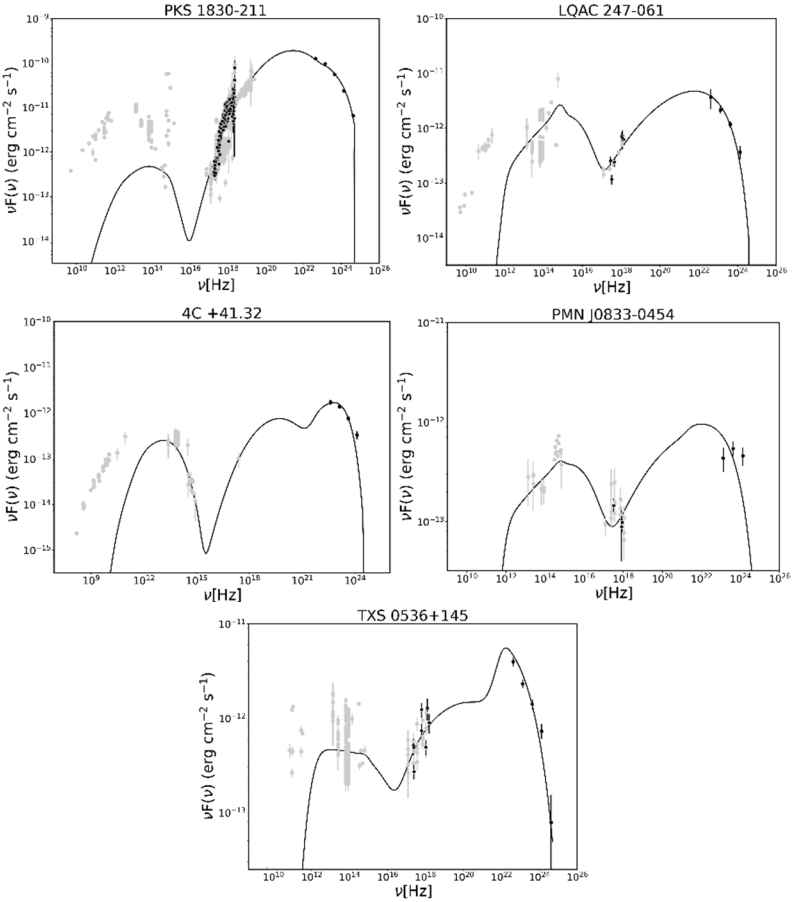

Figure 9. The modeling of multiwavelength SEDs of considered sources.

those two sources, $(12.94 \pm 1.82) \times 10^3$ and $(8.57 \pm 0.76) \times 10^3$ respectively.The cut-off energy is estimated to be $(5.99 \pm 0.41) \times 10^3$, $(2.75 \pm 0.27) \times 10^3$ and $(1.62 \pm 0.14) \times 10^3$ for PKS 1830-211, LQAC 247-061 and 4C+41.32 respectively. The modeling shows that the magnetic field in the emitting region is within $0.1 - 15.8$ G where the lowest magnetic field of 0.1 ± 0.01 G is estimated for PKS 1830-211 while maximum of 15.82 ± 1.74 for LQAC 247-061. For the considered sources, the Doppler boosting factor varies in a small range of $12.28 - 14.58$ which is typical value usually estimated for the FSRQs. The modeling allowed to estimate also variability time or the size of the emitting region. The variability time is order to sub-day scales for all the considered except for 4C +41.31 for which $t_{var} = 3.73$ days which corresponds to $R = 3.37 \times 10^{16}$ cm considering its redshift of $z = 2.55$.

For all the considered sources, the jet is particle dominated with $L_e/L_B > 1$. The highest total luminosity of $L_{tot} = L_e + L_B = 3.17 \times 10^{46}$ erg s^{-1} is estimate for PKS 1830-211 while

PMN J0833-0454 has the lowest luminosity of 5.52×10^{44} erg s^{-1}. The modeling allows to put un upper limit on the disk luminosity requiring that it does not overproduce the synchrotron component. The disc luminosity varies in the range of $(0.01 - 9) \times 10^{46}$ erg s^{-1}.

Publications in the topic of thesis

1. N. Sahakyan, D. Israyelyan, G. Harutyunyan, M. Khachatryan, S. Gasparyan, "Multiwavelength study of high-redshift blazars", *Monthly Notices of the Royal Astronomical Society*, Volume 498, Issue 2, October 2020, Pages 2594–2613.
2. N. Sahakyan, G. Harutyunyan, D. Israyelyan, "Origin of multiwavelength emission from flaring high redshift blazar PKS 0537–286", *Monthly Notices of the Royal Astronomical Society*, Volume 521, Issue 1, May 2023, Pages 1013–1022.
3. Sahakyan N., Harutyunyan G., Israyelyan D., and Khachatryan M., "Exploring the Origin of Multiwavelength Emission from High-Redshift Blazar B3 1343+451", Astrophysics, vol. 63, no. 3, pp. 334–348, 2020.
4. Harutyunyan G., "Multiwavelength Propertirs of Selected High-Redshift blazars", Astrophysics, vol. 66, no. 2, pp. 195-209, 2023.
5. G. Harutyunyan and D. Israyelyan, "Multiwavelength study of high-redshift blazars", Marcel Grosman proceedings, pp. 445-461, 2023.

ԱՄՓՈՓԱԳԻՐ

Ակտիվ գալակտիկական միջուկները (ԱԳՄ-ները) ոչ ջերմային ճառագայթմամբ հզոր աղբյուրներ են՝ էլեկտրամագնիսական սպեկտրի ողջ տիրույթում: Ըստ ԱԳՄ-ների միասնական տեսության, բոլոր ԱԳՄ-ներն ունեն համանման ներքին կառուցվածք, որոնց դիտողական հատկությունների տարբերությունը կախված է աղբյուրի՝ դիտորդի նկատմամբ ունեցած դիրքից: Օրինակ, երբ ԱԳՄ-ների շիթն ուղղված է դեպի դիտողը, ապա դրանք դասակարգվում են որպես բլազար: Բլազարների ճառագայթումը նկարագրվում է կարճ ժամանակահատվածում ճառագայթման կտրուկ փոփոխականությամբ էլեկտրամագնիսական սպեկտրի բոլոր տիրույթներում, բարձր լուսատվությամբ, ռադիո և օպտիկական տիրույթներում ճառագայթման բևեռացվածությամբ և այլն: Մեծ լուսատվության պատճառով բլազարները հայտնաբերվել են նույնիսկ մեծ հեռավորությունների վրա, ուստի դրանց ուսումնասիրումը առանձնահատուկ հետաքրքրություն է ներկայացնում: Ատենախոսության հիմնական նպատակն է ուսումնասիրել բարձր էներգիաների գամմա տիրույթում գրանցված մեծ կարմիր շեղումով բլազարների բազմաալիքային տիրույթում ճառագայթման մեխանիզմները: Ատենախոսությունը կազմված է ներածությունից, հինգ գլուխներից, վերջաբանից և հղումների ցանկից:

Առաջաբանում ներկայացված է թեմային առնչվող գիտական գրականության

համառոտ ակնարկ, թեմայի արդիականությունը և գիտական նորույթը։

Առաջին գլխում հակիրճ ներկայացվել է Fermi-LAT դիտակով գրանցված տվյալների մշակման հիմնական սկզբունքները, ինչպես նաև՝ բլազարների շիթերում հիմնական ճառագայթման մեխանիզմները։

Երկրորդ գլխում քննարկվել է բարձր էներգիանների գամա տիրույթում գրանցված 33 հեռավոր բլազարների ($z > 2.5$) ճառագայթման սպեկտրալ և ժամանակային հատկությունները վերլուծելով Fermi-LAT և Swift դիտակներով գրանցված տվյալները։

Երրորդ գլխում ներկայացված է PKS 0537-286 ($z = 3.1$) բլազարի շիթից ճառագայթման մեխանիզմների համապարփակ ուսումնասիրությունը։ Աղբյուրի բազմահաճախային սպեկտրի էներգիական բաշխվածությունը մոդելավորվել է հանգիստ և ակտիվ վիճակներում՝ մեկ տիրույթից լեպտոնային մոդելի շրջանակում, գնահատվել են շիթը նկարագրող հիմնական պարամետրերը։

Չորրորդ գլխում ուսումնասիրվել է մեծ հեռավորությամբ B3 1343+451 բլազարի ճառագայթումը բազմաալիքային տիրույթում։ Վերջին տարիներին գամմա տիրույթում աղբյուրը եղել է ակտիվ ճառագայթման վիճակում։ Իրականացնելով գամմա տիրույթում գրանցված տվյալների ժամանակային վերլուծություն, գնահատվել է ճառագայթման տիրույթի չափը։

Հինգերորդ գլխում քննարկվել են մեծ հեռավորությամբ ($z > 2.5$) 7 բլազարների շիթերում տեղի ունեցող ոչ-ջերմային պրոցեսները։ Աղբյուրների ճառագայթման սպեկտրները մոդելավորվել են մեկ տիրույթից լեպտոնային տեսության շրջանակում հակադարձ կոմպտոնյան ցրման համար, հաշվի առնելով և՛ սինքրոտրոնային, և՛ արտաքին ֆոտոնային դաշտերը։ Գնահատվել են ճառագայթող մասնիկները նկարագրող պարամետրերը և շիթի լուսատվությունը։

Резюме

Активные ядра галактик (АЯГ) являются источниками мощного нетеплового излучения во всем диапазоне электромагнитного спектра. Согласно единой теории АЯГ, все АЯГ имеют схожую внутреннюю структуру, а различие в наблюдательных свойствах зависит от положения источника относительно наблюдателя. Например, когда струя АЯГ направлена на наблюдателя, они классифицируются как блазары. Излучение блазаров характеризуется резкой изменчивостью излучения за короткий промежуток времени во всех диапазонах электромагнитного спектра, высокой светимостью, поляризацией излучения в радио и оптическом диапазонах и др. Благодаря высокой яркости блазары обнаруживаются даже на больших расстояниях, следовательно изучение этих объектов представляет особый интерес. Основной целью

диссертации является многоволновие исследование механизмов излучения блазаров зарегистрированных в γ-диапазоне высоких энергий с большим красным смещением.

Диссертация состоит из введения, пяти глав, заключения и списка литературы. Во введении произведен обзор научной литературы, касающейся данной темы, а также изложены актуальность и цели исследования.

В главе 1 кратко представлены основные принципы обработки данных зарегистрированных с помощью Fermi-LAT а также основные механизмы излучения в струях блазаров.

В главе 2 рассмотрены спектрально-временные свойства излучения 33 далеких блазаров ($z > 2.5$), зарегистрированных в высокоэнергетическом γ-диапазоне, путем анализа данных, зарегистрированных с помощью телескопов Fermi-LAT и Swift.

В главе 3 представлено всестороннее исследование механизмов излучения из струи блазара PKS 0537-286($z = 3.1$). В рамках однозонной лептонной модели смоделировано многоволновое спектральное распределение энергии источника в спокойном и активном состояниях и оценены основные параметры, описывающие струи блазара.

В главе 4 исследовано излучение дальнего блазара B3 1343+451 в многоволновом диапазоне. В последние годы источник находится в состоянии активного излучения в γ-диапазоне. Путем проведения временного анализа данных, зарегистрированных в γ-диапазоне, был оценен размер излучающей области.

В главе 5 обсуждены нетепловые процессы, происходящие в струях 7 блазаров на большом расстоянии ($z > 2.5$). Спектры излучений источников были моделированы в рамках однозонной лептонной модели, предполагая, что излучение возникает за счет синхротронных фотонов и обратного комптоновского рассеяния как синхротронных, так и внешних фотонов. Оценены параметры, описывающие излучающие частицы и светимость струи.

Gevorg Harutyunyan/ Գևորգ Հարությունյան/ Геворг Арутюнян_____